



Enhancing interfacial electric field in $\text{WO}_3\text{-C}_3\text{N}_4$ through fermi level modulation for electrocatalytic nitrogen reduction

Xiaoxuan Wang^a, Jiangzhou Xie^b, Shuyuan Li^a, Zhi Yuan^a, Yanfei Sun^a, Xueying Gao^a, Zheng Tang^a, Huiying Zhang^a, Jingxian Li^a, Shiyu Wang^a, Zhiyu Yang^{a,*}, Yi-Ming Yan^{a,*}

^a State Key Lab of Organic-Inorganic Composites, Beijing Advanced Innovation Center for Soft Matter Science and Engineering, Beijing University of Chemical Technology, Beijing 100029, People's Republic of China

^b School of Mechanical and Manufacturing Engineering, University of New South Wales, Sydney, New South Wales 2052, Australia



ARTICLE INFO

Keywords:

Electrochemical nitrogen reduction
Fermi level gap
Interfacial electric field
O vacancy
Adsorption and activation of N_2

ABSTRACT

The electrocatalytic nitrogen reduction reaction (ENRR) has been identified as a promising method for environmentally friendly NH_3 production under ambient conditions. The interfacial electric field has been found to hold significant potential for enhancing ENRR performance. The as-prepared $\text{WO}_3\text{-C}_3\text{N}_4\text{-R}$ catalyst exhibited a promising NH_3 yield of $43.5 \mu\text{g h}^{-1} \text{mg}_{\text{cat}}^{-1}$ and a high FE of 11.2 % in 0.1 M Li_2SO_4 . DFT calculations indicate that the enlarged Fermi level can induce more electrons transfer from WO_3 to C_3N_4 to form a strong interfacial electric field. *In situ* Raman and FTIR spectra demonstrate that the engineered intensified interfacial electric field in $\text{WO}_3\text{-C}_3\text{N}_4\text{-R}$ can enhance the adsorption of N_2 molecules by forming strong W-N bonds and the polarization of $\text{N}=\text{N}$ bond through an "acceptance-donation" mechanism, resulting in a promoted ENRR kinetics. This work demonstrates a novel strategy to design NERR catalysts and provides insights into the effects of interfacial electric field on NERR.

1. Introduction

Ammonia (NH_3) is a crucial chemical feedstock and energy carrier for the agricultural and chemical industries [1–6]. However, the traditional Haber-Bosch process used to synthesize NH_3 requires high temperature and pressure conditions [7–11], leading to excessive energy consumption and carbon dioxide (CO_2) emissions [12–15]. To overcome these challenges, the electrocatalytic nitrogen reduction reaction (ENRR) has emerged as a potential "green" NH_3 production method [16–20]. Unfortunately, the efficiency of NH_3 production through ENRR is largely limited by two critical bottlenecks: nitrogen adsorption and activation at the electrocatalyst surface [21,22].

Recently, interfacial electric field, which can accumulate reactants, facilitate electron exchange between electrocatalysts and adsorbent, and regulate the thermodynamic barriers of reactions, has been extensively studied to enhance the performances of ENRR catalysts [23–26]. For instance, our previous work reported that the strong interfacial electric field in $\text{CoO}\text{-Co}_3\text{O}_4$ effectively boosted the adsorption and activation of N_2 , resulting in a high NH_3 yield of $59.96 \mu\text{g h}^{-1} \text{mg}_{\text{cat}}^{-1}$ [27]. Tang et al. constructed an electric field on the h-BN surface to promote N_2

adsorption and weaken the $\text{N}\equiv\text{N}$ bond [28]. One effective method for enhancing the interfacial electric field is through Fermi level modulation in a heterogeneous catalyst. The larger Fermi level gap between two semiconductor materials, the more uneven the distribution of charge in the heterojunction, leading to a stronger interfacial electric field. For example, Yue et al. enlarged Fermi level gap between BiVO_4 and CsPbBr_3 , yielding an enhanced interfacial electric field to promote photocatalytic CO_2 reduction [29]. Zhang et al. utilized a bilateral interface modification method to enlarge the Fermi level gap between the surface and bottom layers, leading to a reinforced interfacial electric field that boosted separation and oriented transport of carriers inside the perovskite film [30]. Despite the promising results of Fermi level modulation in enhancing the interfacial electric field in various catalyst systems, its potential for promoting heterogeneous ENRR catalysts has been relatively underexplored.

In this work, we focused on the construction of a $\text{WO}_3\text{-C}_3\text{N}_4$ heterostructure and employed a strategy of tuning the O vacancy concentration in WO_3 to widen the Fermi level gap between WO_3 and C_3N_4 , resulting in an intensified interfacial electric field. We discovered that increasing the O vacancy concentration in WO_3 can shift the Fermi level

* Corresponding authors.

E-mail addresses: yangzhiyu@mail.buct.edu.cn (Z. Yang), yanym22@mail.buct.edu.cn (Y.-M. Yan).

of WO_3 upwards and hence expand the Fermi level gap between WO_3 and C_3N_4 . As a result, the prepared $\text{WO}_3\text{-C}_3\text{N}_4\text{-R}$ catalyst, with higher O vacancy concentration and stronger interfacial electric field, displayed an elevated NH_3 yield of $43.5 \mu\text{g h}^{-1} \text{mg}_{\text{cat}}^{-1}$ at -0.3 V vs RHE, which was significantly higher than that of the $\text{WO}_3\text{-C}_3\text{N}_4\text{-P}$ catalyst with lower O vacancy concentration and weaker interfacial electric field. Zeta potential and Kelvin probe force microscopy (KPFM) were utilized to prove the intensified interfacial electric field in $\text{WO}_3\text{-C}_3\text{N}_4\text{-R}$ heterostructure. Additionally, *in situ* experiments and density functional theory (DFT) calculations affirmed that the intensified interfacial electric field provided a strong drive force to promote the adsorption and activation of N_2 molecules on the electrocatalyst surface, leading to the observed increase in NH_3 yield. This study highlights the tremendous potential of

designing efficient ENRR electrocatalysts through Fermi level modulation, thereby enhancing the interfacial electric field in the heterostructure, and reveals the underlying mechanism of enhanced ENRR by the interfacial electric field.

2. Experimental section

2.1. Preparation of electrocatalysts

In brief, WO_3 was prepared by calcination of commercial WS_2 at $800 \text{ }^\circ\text{C}$ for 2 h in air atmosphere. Subsequently, 45 mg WO_3 was dispersed in 10 mL methanol and then 1 mL $0.1 \text{ mol L}^{-1} \text{NaBH}_4$ solution was added. The obtained solution was kept stirring for another 30 min.

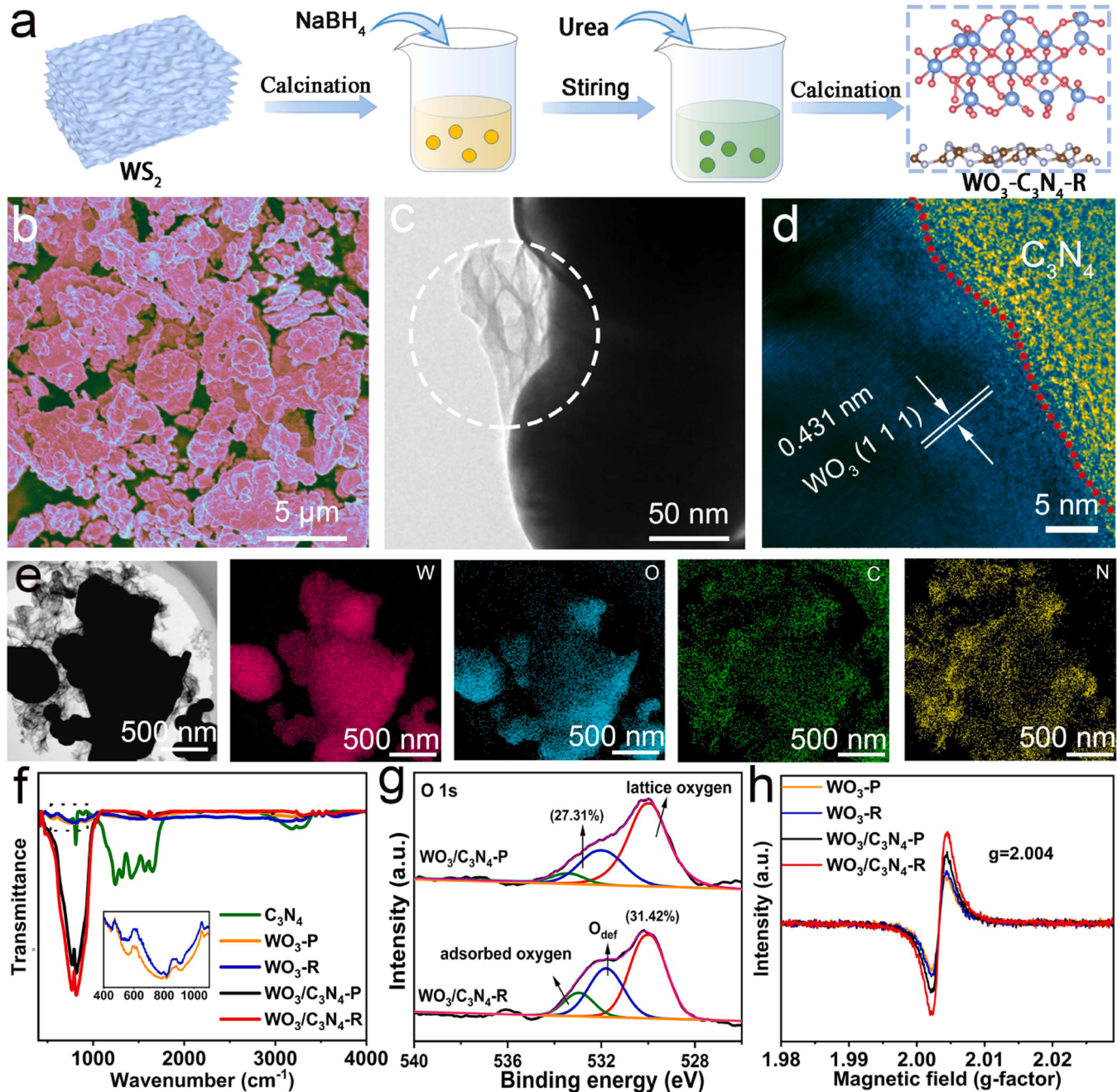


Fig. 1. (a) Schematic diagram of the $\text{WO}_3\text{-C}_3\text{N}_4\text{-R}$ synthesis. (b) SEM image of $\text{WO}_3\text{-C}_3\text{N}_4\text{-R}$; (c) TEM image of $\text{WO}_3\text{-C}_3\text{N}_4\text{-R}$. (d) HRTEM image of the selected region in (c). (e) EDS mapping results of $\text{WO}_3\text{-C}_3\text{N}_4\text{-R}$. (f) FTIR spectra of all samples. (g) O 1s spectra of $\text{WO}_3\text{-C}_3\text{N}_4\text{-P}$ and $\text{WO}_3\text{-C}_3\text{N}_4\text{-R}$. (h) EPR spectra of $\text{WO}_3\text{-P}$, $\text{WO}_3\text{-R}$, $\text{WO}_3\text{-C}_3\text{N}_4\text{-P}$ and $\text{WO}_3\text{-C}_3\text{N}_4\text{-R}$.

The excess solution was removed by vacuum filtration. The obtained products were dried at 60 °C for 24 h and named as $\text{WO}_3\text{-R}$. $\text{WO}_3\text{-P}$ was prepared using the same method without the addition of NaBH_4 . Subsequently, 0.1 g of $\text{WO}_3\text{-R}$ and 0.1 g of urea were meticulously ground and mixed. This amalgamation was then relocated to a horizontal tube furnace and heated to 500 °C at a rate of 5 °C min⁻¹ under a nitrogen atmosphere and kept at 500 °C for 120 min. After cooling to ambient temperature, the $\text{WO}_3\text{-C}_3\text{N}_4\text{-R}$ was successfully synthesized. The $\text{WO}_3\text{-C}_3\text{N}_4\text{-P}$ samples were synthesized with the same process without NaBH_4 .

2.2. Electrochemical measurements

The electrochemical N_2 reduction experiments were carried out using an H-type electrochemical reaction cell. The prepared $\text{WO}_3\text{-C}_3\text{N}_4\text{-R/CP}$ electrode, platinum gauze electrode and Ag/AgCl electrode were used as the working electrode, counter electrode and reference electrode were, respectively. Pure N_2 was continuously injected into electrolyte during the NRR process.

2.3. Characterizations and calculations

The details for characterizations and calculations are provided in the [Supporting information](#).

3. Results and discussion

3.1. Synthesis and characterization of the samples

$\text{WO}_3\text{-C}_3\text{N}_4\text{-R}$ heterostructure was fabricated through a facile method combining calcination and hydrothermal techniques ([Fig. 1a](#)). The same procedure was utilized to fabricate $\text{WO}_3\text{-C}_3\text{N}_4\text{-P}$ catalysts without the addition of NaBH_4 . Furthermore, $\text{WO}_3\text{-R}$ and $\text{WO}_3\text{-P}$ were synthesized through the calcination of WS_2 with and without NaBH_4 , respectively. C_3N_4 was prepared via urea pyrolysis and liquid exfoliation [31]. The scanning electron microscopy (SEM) and transmission electron microscope (TEM) were employed to investigate the morphology of all samples. As displayed in [Fig. 1b](#), [S1](#) and [S2a](#), all samples are composed of sheets without obvious difference. The TEM images demonstrate that the surface of WO_3 is adorned with C_3N_4 , as depicted by the white dotted circles in [Fig. 1c](#) and [S2b](#). The high-resolution TEM (HRTEM) images exhibit that the lattice spacing of WO_3 (111) planes in $\text{WO}_3\text{-C}_3\text{N}_4\text{-R}$ is 0.431 nm, which is higher than that in $\text{WO}_3\text{-C}_3\text{N}_4\text{-P}$ (0.429 nm) ([Fig. 1d](#) and [S2c](#)). It should be noted that the HRTEM images also reveal numerous and close interfacial contacts between the WO_3 and C_3N_4 components. Additionally, the elemental mapping displays a uniform distribution of W, O, C, and N elements within the $\text{WO}_3\text{-C}_3\text{N}_4\text{-R}$ and $\text{WO}_3\text{-C}_3\text{N}_4\text{-P}$ catalysts, as depicted in [Fig. 1e](#) and [S2d](#). X-ray diffraction (XRD) analysis was conducted to investigate the crystal structure of $\text{WO}_3\text{-C}_3\text{N}_4\text{-P}$ and $\text{WO}_3\text{-C}_3\text{N}_4\text{-R}$. As depicted in [Fig. S3](#), the peaks at 23.1°, 24.4°, 26.6°, 34.2° and 41.9° can be attributed to the (002), (200), (202), (120) and (222) planes of WO_3 (JCPDS No. 08-0237), respectively. In addition, two characteristic peaks at 15.9° and 27.4° correspond to the (100) and (110) planes of C_3N_4 (JCPDS No. 50-1250) [32]. To further investigate the chemical bonds of the all samples, Fourier transform infrared (FTIR) analysis was performed. As observed in [Fig. 1f](#), the spectra of $\text{WO}_3\text{-P}$ and $\text{WO}_3\text{-R}$ exhibit broad peaks at 450–900 cm⁻¹, which can be ascribed to the stretching vibration of W-O-W. Regarding the pure C_3N_4 , the peak at 800 cm⁻¹ is assigned to the triazine vibrations, and several characteristic peaks at 1200–1600 cm⁻¹ can be related to the stretching mode of C-N and C=N heterocycles. The absorption peaks located at 3000–3500 cm⁻¹ should be assigned to the amino and surface hydroxyl groups [31]. The above results unequivocally demonstrate the successful synthesis of $\text{WO}_3\text{-C}_3\text{N}_4\text{-P}$ and $\text{WO}_3\text{-C}_3\text{N}_4\text{-R}$ heterostructures, and the existence of a clear interface between WO_3 and C_3N_4 components.

To further investigate the concentration of oxygen vacancies in all

samples, and X-ray photoelectron spectroscopy (XPS) and electron paramagnetic resonance (EPR) were performed. In the XPS spectra, peaks for $\text{WO}_3\text{-C}_3\text{N}_4$ were located at 35.73 and 37.96 eV, corresponding to W^{6+} , while peaks at 34.81 and 37.18 eV were attributed to W^{5+} , which was indicative of oxygen vacancies in WO_3 ([Fig. S4](#)). The peak intensity of W^{5+} in $\text{WO}_3\text{-C}_3\text{N}_4\text{-R}$ was much stronger than that in $\text{WO}_3\text{-C}_3\text{N}_4\text{-P}$ ([Fig. S4](#)), indicating that more oxygen vacancies were formed in $\text{WO}_3\text{-C}_3\text{N}_4\text{-R}$ [33]. Further evidence can be seen in the O 1 s spectrum of samples, which shows that the peaks observed at 530.01, 531.79 and 532.98 eV are attributed to lattice O species, defect oxygen and adsorbed oxygen ([Fig. 1g](#)), respectively [34]. By comparing the fitted peak area, it was found that the relative ratio of oxygen deficiency in $\text{WO}_3\text{-C}_3\text{N}_4\text{-R}$ ($\text{O}_{\text{def}} / (\text{O}_{\text{def}} + \text{O}_{\text{lat}}) = 31.42\%$) was higher than that of $\text{WO}_3\text{-C}_3\text{N}_4\text{-P}$ (27.31 %), indicating a higher concentration of oxygen vacancies in $\text{WO}_3\text{-C}_3\text{N}_4\text{-R}$. Additionally, the intensity of the EPR signal was proportional to the concentration of unpaired electrons in the oxygen vacancy, and a gradual increase in signal intensity at $g = 2.004$ was observed in [Fig. 1h](#), indicating the highest concentration of oxygen vacancies in $\text{WO}_3\text{-C}_3\text{N}_4\text{-R}$ [35,36].

3.2. The electric field analysis of samples

To study the energy band structure of samples, UV/Vis diffuse reflectance spectra (DRS) and Mott-Schottky curves were measured ([Fig. 2a](#) and [c](#)). The band gaps (E_g) of C_3N_4 , $\text{WO}_3\text{-P}$, and $\text{WO}_3\text{-R}$ were calculated to be 2.56, 2.53, and 2.55 eV, respectively, using the Kubelka-Munk equation ([Fig. 2b](#)) [37]. The Mott-Schottky curves showed the flat band potentials (E_{fb}) of C_3N_4 , $\text{WO}_3\text{-P}$, and $\text{WO}_3\text{-R}$ were -1.12 V , -1.29 V , and -1.37 V (vs. Ag/AgCl) ([Fig. 2c](#)), respectively [38,39]. Thus, the conduction band positions of C_3N_4 , $\text{WO}_3\text{-P}$, and $\text{WO}_3\text{-R}$ were calculated to be -1.22 V , -1.39 V , and -1.47 V , respectively. [Fig. 2d](#) and [S5](#) illustrate the band structures of C_3N_4 , $\text{WO}_3\text{-P}$, and $\text{WO}_3\text{-R}$, where the negative shift of the CB positions indicates an upward shift of the Fermi level, leading to an increased Fermi level gap between C_3N_4 and WO_3 .

The enlarged Fermi level gap between two heterostructures can enhance the interfacial electric field due to the increasing difference between the electron affinity and ionization energy. Various measurements were performed to investigate the enhanced interfacial electric field in $\text{WO}_3\text{-C}_3\text{N}_4\text{-R}$. The ultraviolet photoelectron spectra (UPS) results revealed the work functions of C_3N_4 , $\text{WO}_3\text{-P}$, and $\text{WO}_3\text{-R}$ to be 9.26, 8.51, and 7.03 eV ([Fig. 2e](#)), respectively, indicating that $\text{WO}_3\text{-R}$ is more likely to release electrons [40,41]. Zeta potential measurement was conducted to detect the surface charge with results showing that the zeta potential of $\text{WO}_3\text{-C}_3\text{N}_4\text{-R}$ (-34.9 mV) was higher compared to that of $\text{WO}_3\text{-C}_3\text{N}_4\text{-P}$ (-28.1 mV) ([Fig. 2f](#)) [42,43]. Moreover, KPFM was utilized to measure the surface potential of the electrocatalysts [44,45]. [Fig. 2g](#) and [h](#) show the surface potential distribution images of $\text{WO}_3\text{-C}_3\text{N}_4\text{-P}$ and $\text{WO}_3\text{-C}_3\text{N}_4\text{-R}$. The corresponding line-scanning surface potential profiles indicate that the contact potential difference (CPD) of $\text{WO}_3\text{-C}_3\text{N}_4\text{-R}$ (120 mV) was much higher than that of $\text{WO}_3\text{-C}_3\text{N}_4\text{-P}$ (60 mV), demonstrating an intensified interfacial electric field in $\text{WO}_3\text{-C}_3\text{N}_4\text{-R}$. Additionally, we have quantitatively analyzed the intensity of the interfacial electric field by calculating the gradient of the fitted surface potential profiles ([Fig. 2i](#) and [S6](#)), showing that the interfacial electric field intensity of $\text{WO}_3\text{-C}_3\text{N}_4\text{-R}$ ($0.072\text{ V }\mu\text{m}^{-1}$) was higher than that of $\text{WO}_3\text{-C}_3\text{N}_4\text{-P}$ ($0.032\text{ V }\mu\text{m}^{-1}$). The results presented above provide compelling evidence that the enlarged Fermi level gap between WO_3 and C_3N_4 leads to an intensified interfacial electric field in the $\text{WO}_3\text{-C}_3\text{N}_4\text{-R}$ heterostructure. This is expected to be highly advantageous for enhancing the performance of catalysts for ENRR.

3.3. Electrochemical performance

The performances of $\text{WO}_3\text{-C}_3\text{N}_4\text{-P}$ and $\text{WO}_3\text{-C}_3\text{N}_4\text{-R}$ for ENRR were evaluated in a typical H-type cell with 0.1 M Li_2SO_4 as the electrolyte

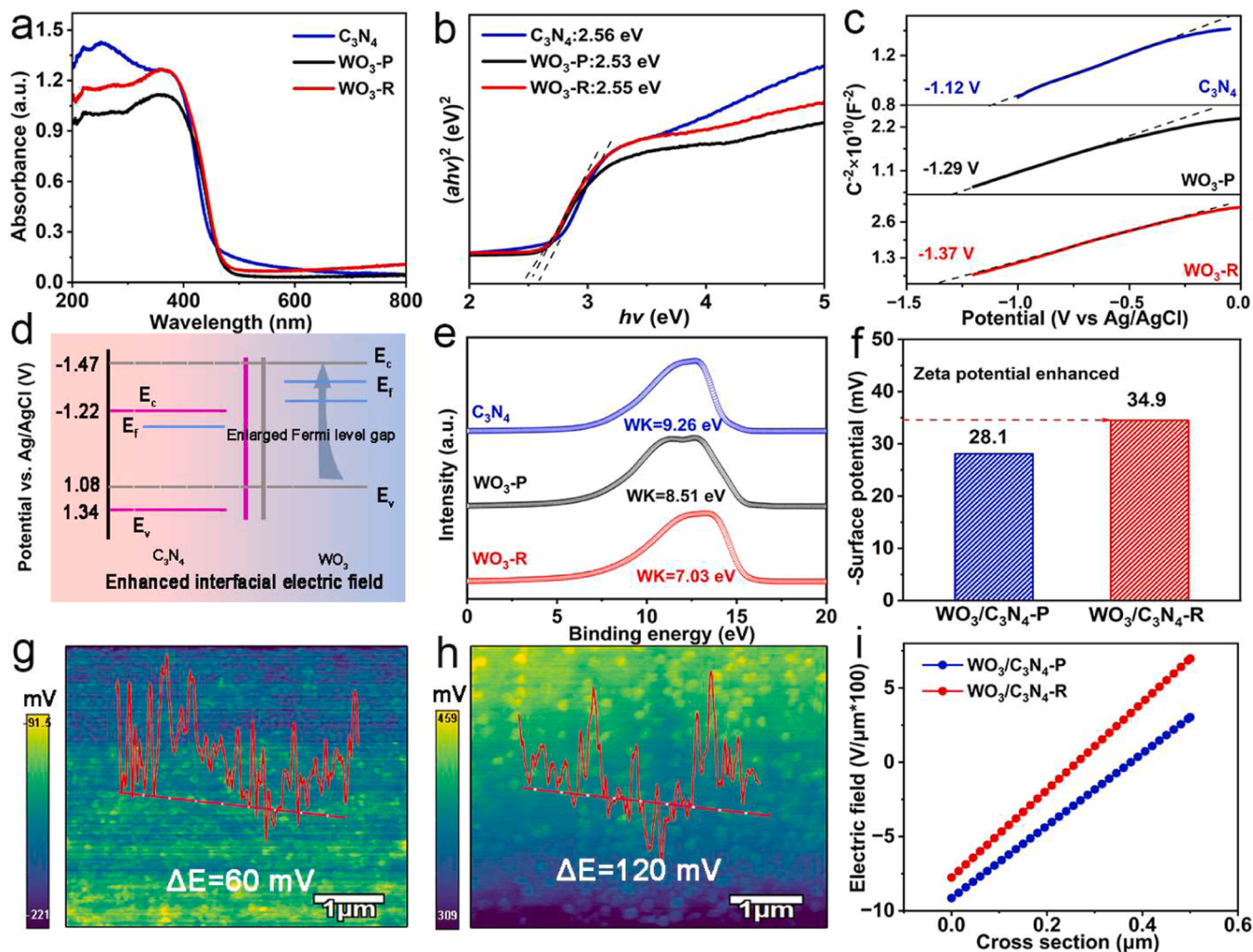


Fig. 2. (a) UV/Vis DRS and (b) Kubelka-Munk plots of C₃N₄, WO₃-P and WO₃-R. (c) Mott-Schottky plots of C₃N₄, WO₃-P and WO₃-R. (d) Illustration of the enlarged Fermi level gap between WO₃ and C₃N₄. (e) Secondary electron cutoff edge of C₃N₄, WO₃-P and WO₃-R acquired by UPS. (f) The Zeta potential of WO₃-C₃N₄-P and WO₃-C₃N₄-R. (g-h) 2D surface potential distributions and corresponding lines canning surface potential profiles of WO₃-C₃N₄-P and WO₃-C₃N₄-R. (i) The intense distributions of interfacial electric field on WO₃-C₃N₄-P and WO₃-C₃N₄-R surfaces.

(Figs. S7 and S8). Initially, the N₂ gas, inclusive of the isotope gas utilized in this study, was purified. The comprehensive process detailing this procedure is available in the methods section. As substantiated by the UV-vis absorption spectra (Fig. S9), no traces of NH₃ or NO_x contaminants were detected in the purified gas. The linear sweep voltammetry (LSV) curves of WO₃-C₃N₄-R (Fig. 3a) showed a higher reduction current density in N₂-saturated (99.99%) electrolyte than in Ar-saturated electrolyte, indicating that the catalytic reduction of N₂ to NH₃ occurred on the surface of WO₃-C₃N₄-R. Moreover, the high selectivity of WO₃-C₃N₄-R was demonstrated as no N₂H₄ was detected (Fig. 3b and S10). The NH₃ yields were determined by UV-vis absorption spectra and the Faradaic efficiencies (FEs) were calculated according to chronoamperometry results (Figs. S11-13) [46,47]. A series of control experiments were conducted to exclude any possible interference from contaminants with results showing that no NH₃ products were detected in any of the control conditions (Fig. 3c). The NH₃ yields and FEs at applied potentials ranging from -0.1 to -0.5 V were measured and compared between the WO₃-C₃N₄-P and WO₃-C₃N₄-R electrocatalysts. As shown in Fig. 3d and e, WO₃-C₃N₄-R exhibited an NH₃ yield of 43.5 $\mu\text{g h}^{-1} \text{mg}_{\text{cat}}^{-1}$ and FE of 11.2 % at -0.3 V vs RHE, which were significantly higher than those of WO₃-C₃N₄-P (38.4 $\mu\text{g h}^{-1} \text{mg}_{\text{cat}}^{-1}$ and 4.2 %, respectively). Simultaneously, ion chromatograph (IC) (Fig. S14) detected the ammonia yield for the WO₃-C₃N₄-R under

optimized condition to be 42.3 $\mu\text{g h}^{-1} \text{mg}_{\text{cat}}^{-1}$, which was in close consistent with the colorimetric result (43.5 $\mu\text{g h}^{-1} \text{mg}_{\text{cat}}^{-1}$). Therefore, the IC results testified that the results by spectrophotometry is reliable. To assess the electrochemical stability of WO₃-C₃N₄-R, consecutive recycling electrolysis was performed at -0.3 V vs RHE (Fig. 3f). The NH₃ yield and FE of the WO₃-C₃N₄-R electrocatalyst remained almost unchanged during five consecutive cycles (each lasts two hours), implying the excellent stability of WO₃-C₃N₄-R. Furthermore, the FTIR, XRD, HRTEM and XPS were performed to verify the structure stability of WO₃-C₃N₄-R (Figs. S15 and S16). There was no discernible structural alteration of WO₃-C₃N₄-R observed for the ENRR, signifying its commendable structural durability. In addition, the obtained performance of WO₃-C₃N₄-R was superior to that of most recently reported ENRR electrocatalysts (Table S1). Furthermore, to investigate the source of the produced NH₃, isotopic labeling experiments (Fig. 3g) were conducted using ¹⁵N₂ (99 atom% ¹⁵N) and ¹⁴N₂ as the feeding gas. ¹H nuclear magnetic resonance (¹H NMR) spectra revealed a double coupling and a triplet coupling for ¹⁵NH₄⁺ and ¹⁴NH₄⁺ when using ¹⁵N₂ and ¹⁴N₂ as the feeding gas, respectively, indicating that the generated NH₃ originated from ENRR [48]. The capacitances of the samples, which were proportional to the electrochemically active surface areas (ECSAs), were determined by measuring CV curves at different scan rates (Fig. S17). The WO₃-C₃N₄-R sample showed a larger capacitance of

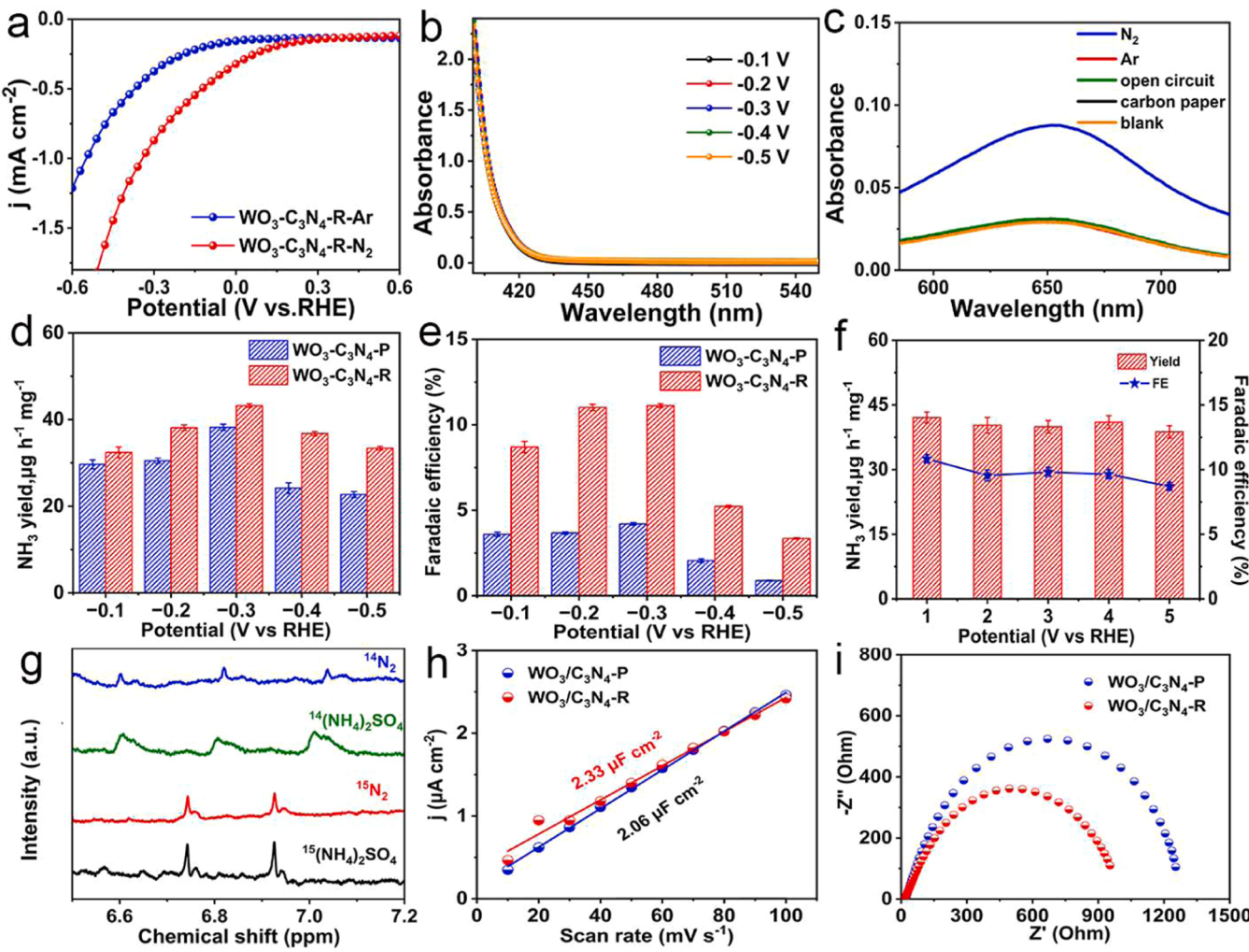


Fig. 3. (a) LSV curves of $\text{WO}_3\text{-C}_3\text{N}_4\text{-R}$ in Ar-saturated and N_2 -saturated 0.1 M Li_2SO_4 . (b) UV-Vis absorption spectra of the electrolytes with the Watt and Chrissp's method. (c) UV-vis absorption spectra at different control conditions. (d) NH_3 yield of $\text{WO}_3\text{-C}_3\text{N}_4\text{-P}$ and $\text{WO}_3\text{-C}_3\text{N}_4\text{-R}$. (e) Faradaic efficiency of $\text{WO}_3\text{-C}_3\text{N}_4\text{-P}$ and $\text{WO}_3\text{-C}_3\text{N}_4\text{-R}$. (f) Cycling test for $\text{WO}_3\text{-C}_3\text{N}_4\text{-R}$ at -0.3 V vs RHE. (g) ^1H NMR spectra of $\text{WO}_3\text{-C}_3\text{N}_4\text{-R}$ fed by $^{14}\text{N}_2$ and $^{15}\text{N}_2$ gas. (h) C_{dl} measurement of $\text{WO}_3\text{-C}_3\text{N}_4\text{-P}$ and $\text{WO}_3\text{-C}_3\text{N}_4\text{-R}$ in 0.1 M Li_2SO_4 electrolyte. (i) Nyquist plots of $\text{WO}_3\text{-C}_3\text{N}_4\text{-P}$ and $\text{WO}_3\text{-C}_3\text{N}_4\text{-R}$ in 0.1 M Li_2SO_4 electrolyte.

$2.33 \mu\text{F cm}^{-2}$ compared to $\text{WO}_3\text{-C}_3\text{N}_4\text{-P}$ ($2.06 \mu\text{F cm}^{-2}$) (Fig. 3h) with results indicating that the $\text{WO}_3\text{-C}_3\text{N}_4\text{-R}$ had more active sites, which should contribute to the higher oxygen vacancy concentration in $\text{WO}_3\text{-C}_3\text{N}_4\text{-R}$. Besides, electrochemical impedance spectroscopy (EIS) was performed and the results showed that $\text{WO}_3\text{-C}_3\text{N}_4\text{-R}$ possessed a lower R_{ct} value compared to $\text{WO}_3\text{-C}_3\text{N}_4\text{-P}$, indicating better charge transfer kinetics of $\text{WO}_3\text{-C}_3\text{N}_4\text{-R}$ (Fig. 3i).

3.4. In situ measurements and DFT calculation

DFT calculations were further conducted to investigate the intensified interfacial electric field and charge transfer in $\text{WO}_3\text{-C}_3\text{N}_4\text{-R}$ heterostructure. The model $\text{WO}_3\text{-C}_3\text{N}_4\text{-P}$ and $\text{WO}_3\text{-C}_3\text{N}_4\text{-R}$ under different views were presented in Fig. S18. Firstly, electrostatic potential was used to illustrate the intensity of interfacial electric field in $\text{WO}_3\text{-C}_3\text{N}_4\text{-P}$ and $\text{WO}_3\text{-C}_3\text{N}_4\text{-R}$ (Fig. 4a and d). The results indicated that the $\text{WO}_3\text{-C}_3\text{N}_4\text{-R}$ exhibited a larger ΔV_{et} of 13.03 eV compared to $\text{WO}_3\text{-C}_3\text{N}_4\text{-P}$ of 12.23 eV , indicating a stronger interfacial electric field in $\text{WO}_3\text{-C}_3\text{N}_4\text{-R}$ [49,50]. Furthermore, the difference charge density was used to explore the charge transfer between WO_3 and C_3N_4 . It was observed that 2.52 e^- was transferred from WO_3 to C_3N_4 at the interface of $\text{WO}_3\text{-C}_3\text{N}_4\text{-R}$, which was larger than $\text{WO}_3\text{-C}_3\text{N}_4\text{-P}$ (1.73 e^-) (Fig. 4b and e). Moreover, Fig. 4c and f show the plane-averaged charge density difference of

$\text{WO}_3\text{-C}_3\text{N}_4\text{-P}$ and $\text{WO}_3\text{-C}_3\text{N}_4\text{-R}$ along the z-direction [51–53]. The red and blue regions correspond to electron accumulation and depletion, respectively. It can be observed that a notable charge transfer occurs from WO_3 to C_3N_4 in both the $\text{WO}_3\text{-C}_3\text{N}_4\text{-P}$ and $\text{WO}_3\text{-C}_3\text{N}_4\text{-R}$ heterostructure models, which is consistent with the UPS results.

N_2 temperature-programmed desorption ($\text{N}_2\text{-TPD}$) was conducted to evaluate the N_2 adsorption behaviors of $\text{WO}_3\text{-C}_3\text{N}_4\text{-P}$ and $\text{WO}_3\text{-C}_3\text{N}_4\text{-R}$. N_2 desorption peak of $\text{WO}_3\text{-C}_3\text{N}_4\text{-R}$ was observed at $565.3 \text{ }^\circ\text{C}$, which was notably stronger than that of $\text{WO}_3\text{-C}_3\text{N}_4\text{-P}$ ($554.8 \text{ }^\circ\text{C}$) (Fig. S19). This result suggests that the intensified interfacial electric field in $\text{WO}_3\text{-C}_3\text{N}_4\text{-R}$ can significantly enhance the chemical adsorption of N_2 , leading to an improved ENRR kinetics [54,55]. To further investigate the N_2 -catalyst interactions, in situ Raman and FTIR measurements were conducted. The results showed a significant W-N vibrational band at 800 cm^{-1} in $\text{WO}_3\text{-C}_3\text{N}_4\text{-R}$ (Fig. 4g), indicating that N_2 molecules were strongly adsorbed on the W metal sites. In comparison, $\text{WO}_3\text{-C}_3\text{N}_4\text{-P}$ exhibited a weaker W-N vibration band (Fig. S20), indicating a weaker adsorption capacity of N_2 [56]. Additionally, the nitrogen adsorption peak exhibited a noticeable blueshift in $\text{WO}_3\text{-C}_3\text{N}_4\text{-R}$ (1235.27 cm^{-1}) compared to $\text{WO}_3\text{-C}_3\text{N}_4\text{-P}$ (1245.62 cm^{-1}) (Fig. 4h), which suggested an enlarged $\text{N}\equiv\text{N}$ bond when N_2 was adsorbed on the surface of $\text{WO}_3\text{-C}_3\text{N}_4\text{-R}$ [57]. Based on these observations, it can be assumed that the intensified interfacial electric field could enhance the adsorption of N_2 and activate

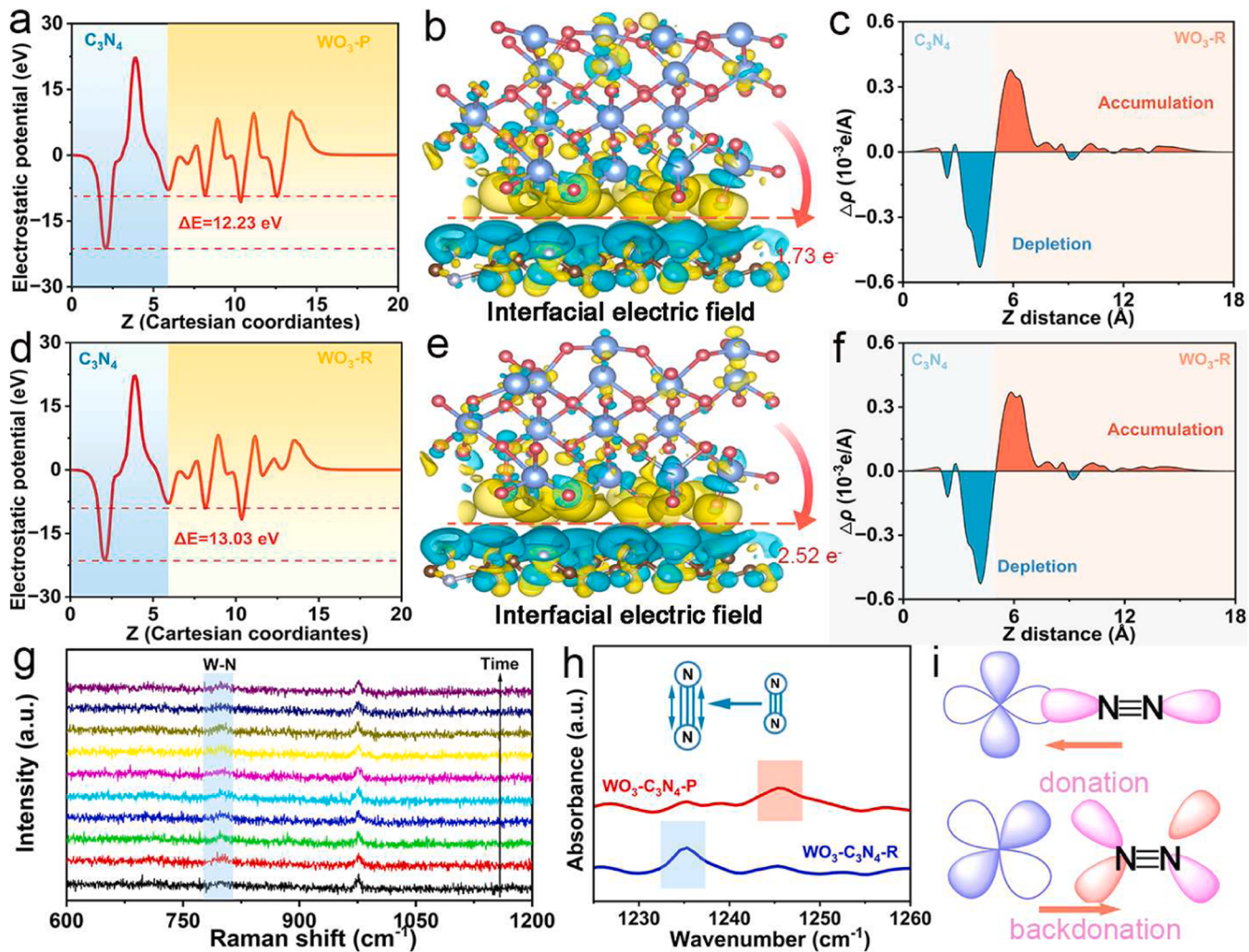


Fig. 4. (a) Electrostatic potential profile of $\text{WO}_3\text{-C}_3\text{N}_4\text{-P}$. (b) The DCD of the $\text{WO}_3\text{-C}_3\text{N}_4\text{-P}$. (c) Plane-averaged charge density difference for $\text{WO}_3\text{-C}_3\text{N}_4\text{-P}$ along z-direction. (d) Electrostatic potential profile of $\text{WO}_3\text{-C}_3\text{N}_4\text{-R}$. (e) The DCD of the $\text{WO}_3\text{-C}_3\text{N}_4\text{-R}$. (f) Plane-averaged charge density difference for $\text{WO}_3\text{-C}_3\text{N}_4\text{-R}$ along z-direction. (g) *In situ* Raman spectrum of the $\text{WO}_3\text{-C}_3\text{N}_4\text{-R}$ at -0.3 V in $0.1 \text{ M Li}_2\text{SO}_4$. (h) *In situ* FTIR spectra of $\text{WO}_3\text{-C}_3\text{N}_4\text{-P}$ and $\text{WO}_3\text{-C}_3\text{N}_4\text{-R}$. (i) Schematic of electron feedback mechanism from d orbitals of W to π^* of N_2 .

the $\text{N}\equiv\text{N}$ triple bond more efficiently to accelerate ENRR. Fig. 4i illustrates the "acceptance-donation" mechanism, in which the empty d orbitals of the W atom accept lone-pair electrons of the N_2 molecule. In turn, the occupied d orbital can donate electrons to the π^* orbital of N_2 , thereby weakening the $\text{N}\equiv\text{N}$ bond and activating the N_2 molecule, which facilitates its conversion into NH_3 .

To gain deeper insight into the effect of the intensified interfacial electric field on N_2 adsorption and activation, we compared the geometrical structures of N_2 adsorbed on $\text{WO}_3\text{-C}_3\text{N}_4\text{-P}$ and $\text{WO}_3\text{-C}_3\text{N}_4\text{-R}$. The calculated bond lengths of W-N were 1.952 \AA and 1.919 \AA for $\text{WO}_3\text{-C}_3\text{N}_4\text{-P}$ and $\text{WO}_3\text{-C}_3\text{N}_4\text{-R}$ (Fig. 5a), respectively, indicating a stronger N_2 binding affinity of $\text{WO}_3\text{-C}_3\text{N}_4\text{-R}$ compared to $\text{WO}_3\text{-C}_3\text{N}_4\text{-P}$ [28]. In particular, the $\text{N}\equiv\text{N}$ bond lengthens to 1.154 \AA and 1.157 \AA after adsorption on the surfaces of $\text{WO}_3\text{-C}_3\text{N}_4\text{-P}$ and $\text{WO}_3\text{-C}_3\text{N}_4\text{-R}$ (Fig. 5a), respectively, compared to 1.10 \AA in a free N_2 molecule, suggesting that the enhanced interfacial electric field in $\text{WO}_3\text{-C}_3\text{N}_4\text{-R}$ can effectively elongate and thus activate the $\text{N}\equiv\text{N}$ bond [58]. The distinct bond lengths of W-N and $\text{N}\equiv\text{N}$ in the $\text{WO}_3\text{-C}_3\text{N}_4\text{-R}$ and $\text{WO}_3\text{-C}_3\text{N}_4\text{-P}$ models can be attributed to the electron transfer that occurs between the catalysts and the adsorbed N_2 molecules during ENRR. When the N_2 molecules are adsorbed onto the catalyst surface, they become polarized and form a weak bond with the catalyst atoms. This polarization induces a redistribution of electron density in the system, resulting in a transfer of

electrons from the catalyst to the adsorbed N_2 molecule. This electron transfer can lead to a weakening of the $\text{N}\equiv\text{N}$ bond. Therefore, the charge density differences were measured to investigate the electron transfer from the catalysts to the adsorbed N_2 molecules (Fig. 5b). The calculated electron transfer numbers on the $\text{WO}_3\text{-C}_3\text{N}_4\text{-P}$ and $\text{WO}_3\text{-C}_3\text{N}_4\text{-R}$ models are 0.902 e^- and 1.173 e^- , respectively, suggesting that the intensified interfacial electric field in $\text{WO}_3\text{-C}_3\text{N}_4\text{-R}$ can significantly enhance the ability of the W active site to capture and activate N_2 . Based on the above results, a crystal orbital Hamilton population (COHP) analysis was further performed to investigate the high ENRR kinetics of $\text{WO}_3\text{-C}_3\text{N}_4\text{-R}$ (Fig. 5c) [59–61]. The integrated COHP (ICOHP) value for the W-N bond in the $\text{WO}_3\text{-C}_3\text{N}_4\text{-R}$ model was found to be -6.47 , which was larger than that of $\text{WO}_3\text{-C}_3\text{N}_4\text{-P}$ (-1.94). This suggests that the W-N bond in $\text{WO}_3\text{-C}_3\text{N}_4\text{-R}$ is stronger than that in $\text{WO}_3\text{-C}_3\text{N}_4\text{-P}$. Furthermore, the ICOHP value for the N-N bond in $\text{WO}_3\text{-C}_3\text{N}_4\text{-R}$ was -1.14 , which was slightly lower than that of $\text{WO}_3\text{-C}_3\text{N}_4\text{-P}$ (-1.15). This indicates that the intensified interfacial electric field in $\text{WO}_3\text{-C}_3\text{N}_4\text{-R}$ can significantly weaken the $\text{N}\equiv\text{N}$ bond. The NRR free-energy diagram was utilized to investigate the catalytic activity of $\text{WO}_3\text{-C}_3\text{N}_4\text{-P}$ and $\text{WO}_3\text{-C}_3\text{N}_4\text{-R}$, and the optimized configurations of intermediates are shown in Fig. 5d and S21–23. As shown in Fig. S21, the Gibbs free energy for $^*\text{NH}_2\text{-NH}_3$ to $^*\text{NH}_2$ transformation t is the highest (1.853 eV), identifying it as the potential rate-determining

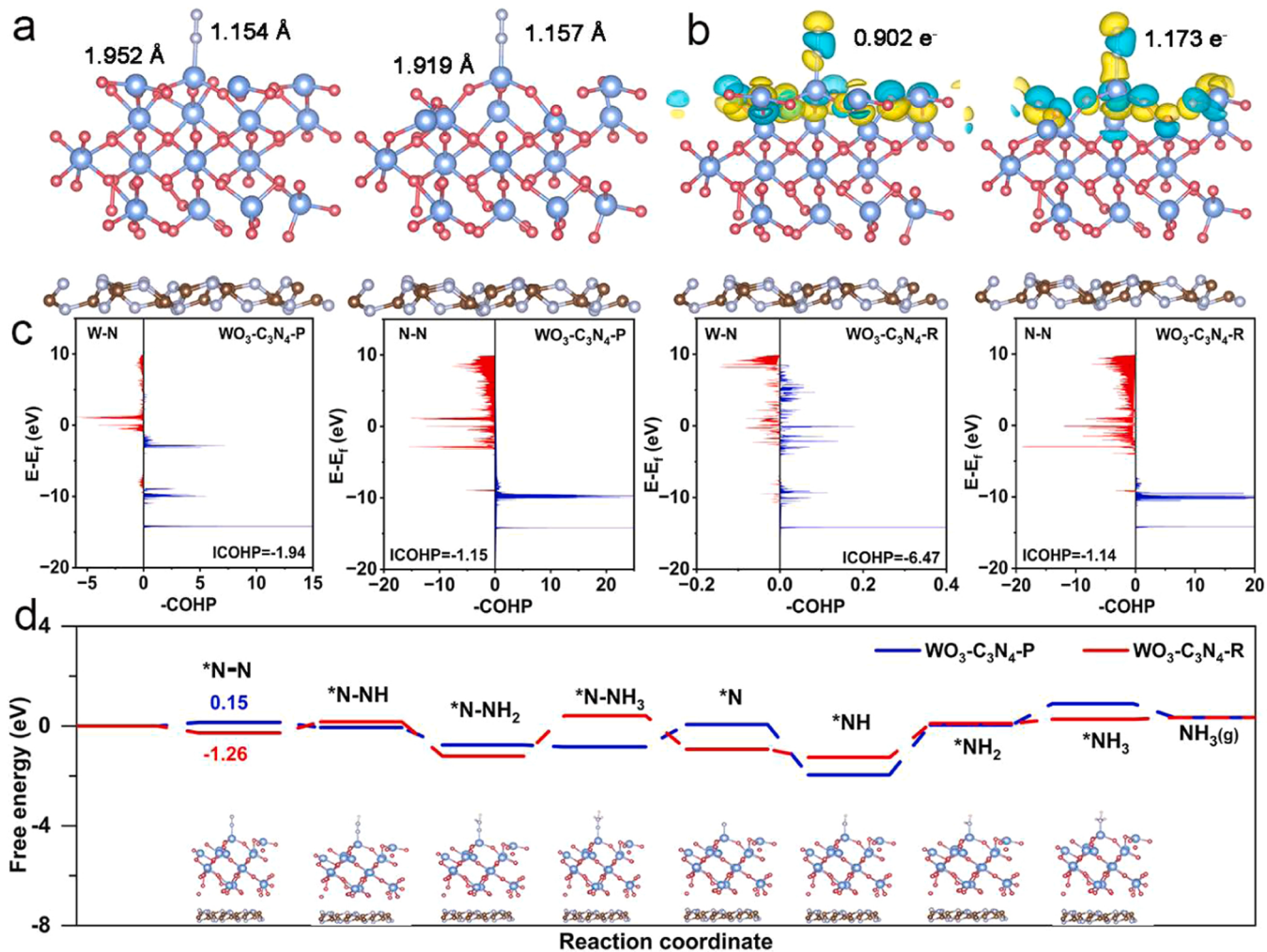


Fig. 5. (a) Optimize structures of N_2 adsorbed on $\text{WO}_3\text{-C}_3\text{N}_4\text{-P}$ (left) and $\text{WO}_3\text{-C}_3\text{N}_4\text{-R}$ (right). (b) Corresponding charge density and the electron transfer value from W to N_2 . (c) The COHP of $\text{WO}_3\text{-C}_3\text{N}_4\text{-P}$ and $\text{WO}_3\text{-C}_3\text{N}_4\text{-R}$. (d) Free energy diagram for NRR of $\text{WO}_3\text{-C}_3\text{N}_4\text{-P}$ and $\text{WO}_3\text{-C}_3\text{N}_4\text{-R}$.

step (RDS) in the alternating mechanism. For the distal mechanism, the RDS involves the conversion of $^*\text{N-NH}_2$ to $^*\text{N-NH}_3$, featuring a relatively lower energy barrier of 1.616 eV. Consequently, it can be deduced that the $\text{WO}_3\text{-C}_3\text{N}_4\text{-R}$ catalyst is more conducive to the distal mechanism in NRR process. Interestingly, the ENRR process on both $\text{WO}_3\text{-C}_3\text{N}_4\text{-P}$ and $\text{WO}_3\text{-C}_3\text{N}_4\text{-R}$ electrocatalysts follows the distal mechanism. The ΔG values for N_2 adsorption are -1.26 eV and 0.15 eV for $\text{WO}_3\text{-C}_3\text{N}_4\text{-R}$ and $\text{WO}_3\text{-C}_3\text{N}_4\text{-P}$, respectively, suggesting that the adsorption of N_2 on $\text{WO}_3\text{-C}_3\text{N}_4\text{-R}$ is energetically favorable, and the enhanced interfacial electric field in $\text{WO}_3\text{-C}_3\text{N}_4\text{-R}$ can optimize the free-energy barrier of N_2 adsorption. With HER serving as the principal competing reaction for the NRR, the HER behaviors of the catalysts were further examined. As shown in Fig. S24, the $\text{WO}_3\text{-C}_3\text{N}_4\text{-R}$ exhibits a higher adsorption free energy of H^* (0.511 eV) compared to $\text{WO}_3\text{-C}_3\text{N}_4\text{-P}$ (0.344 eV), which indicates the $\text{WO}_3\text{-C}_3\text{N}_4\text{-R}$ could effectively suppress the competing HER. Overall, these computational results affirm that the $\text{WO}_3\text{-C}_3\text{N}_4\text{-R}$ electrocatalyst with intensified interfacial electric field is favorable to adsorb and activate N_2 on the electrocatalyst surface, which leads to enhanced ENRR kinetics.

4. Conclusion

To summarize, enlarging Fermi level gap between WO_3 and C_3N_4 by increasing oxygen vacancy concentration in WO_3 can result in an enhanced interfacial electric field in $\text{WO}_3\text{-C}_3\text{N}_4\text{-R}$ heterostructure,

which is demonstrated as an effective strategy of accelerating the ENRR kinetics. Widen Fermi level gap enables more electrons transfer from WO_3 phase to C_3N_4 phase, resulting in an intensified interfacial electric field that providing extra driving force to capture and activate N_2 on W sites. The obtained $\text{WO}_3\text{-C}_3\text{N}_4\text{-R}$ exhibited a high electrochemical nitrogen reduction performance compared to other recently reported catalysts, achieving an excellent NH_3 yield of $43.5 \mu\text{g h}^{-1} \text{mg}_{\text{cat}}^{-1}$ and a reasonable FE of 11.2 % in 0.1 M Li_2SO_4 . This work offers a novel perspective on the modulation of Fermi level to enhance the interfacial electric field in heterostructure for efficient NERR and the insights gained from this work can be extended to the development of new catalysts in other areas.

CRediT authorship contribution statement

Xiaoxuan Wang: Writing original script, data curation, formal analysis, theoretical calculation. **Jiangzhou Xie, Shuyuan Li, Zhi Yuan, Yanfei Sun, Xueying Gao, Zheng Tang, Huiying Zhang, Jingxian Li, Shiyu Wang:** Data collection, analysis and discussion. **Zhiyu Yang, Yi-Ming Yan:** Data discussion, and draft review & editing.

Declaration of Competing Interest

The authors declare that they have no known competing financial interests or personal relationships that could have appeared to influence

the work reported in this paper.

Data availability

No data was used for the research described in the article.

Acknowledgments

Financial support from the National Natural Science Foundation of China (grant nos. 21575016, U20A20154, 22279005) and from the National Program for Support of Top-notch Young Professionals is gratefully acknowledged.

Appendix A. Supporting information

Supplementary data associated with this article can be found in the online version at [doi:10.1016/j.apcatb.2023.123126](https://doi.org/10.1016/j.apcatb.2023.123126).

References

- [1] L. Wen, K. Sun, X. Liu, W. Yang, L.Y. Li, H.L. Jiang, Electronic state and microenvironment modulation of mmetal nanoparticles stabilized by MOFs for boosting electrocatalytic nitrogen reduction, *Adv. Mater.* 35 (2023), 2210669, <https://doi.org/10.1002/adma.202210669>.
- [2] X. Zhang, Y. Lyu, H. Zhou, J. Zheng, A. Huang, J. Ding, C. Xie, R. De Marco, N. Tsud, V. Kalinovich, S.P. Jiang, L. Dai, S. Wang, Photoelectrochemical N₂ to-NH₃ fixation with high efficiency and rates via optimized Si-based system at positive potential versus Li(0/), *Adv. Mater.* (2023), e2211894, <https://doi.org/10.1002/adma.202211894>.
- [3] H. Liu, G. Hai, L.X. Ding, H. Wang, Fluorine-stabilized defective black phosphorene as a lithium-like catalyst for boosting nitrogen electroreduction to ammonia, *Angew. Chem. Int. Ed.* (2023), e202302124, <https://doi.org/10.1002/anie.202302124>.
- [4] H.Y. Zhou, Y.B. Qu, J.C. Li, Z.L. Wang, C.C. Yang, Q. Jiang, Effectively boosting selective ammonia synthesis on electron-deficient surface of MoB₂, *Appl. Catal. B* 305 (2022), <https://doi.org/10.1016/j.apcatb.2021.121023>.
- [5] K. Chu, Y. Luo, P. Shen, X. Li, Q. Li, Y. Guo, Unveiling the synergy of O-vacancy and heterostructure over MoO_{3-x}/MXene for N₂ electroreduction to NH₃, *Adv. Energy Mater.* 12 (2021), 2103022, <https://doi.org/10.1002/aenm.202103022>.
- [6] S. Liu, M. Wang, H. Ji, L. Zhang, J. Ni, N. Li, T. Qian, C. Yan, J. Lu, Solvent-in-gas system for promoted photocatalytic ammonia synthesis on porous framework materials, *Adv. Mater.* 35 (2023), e2211730, <https://doi.org/10.1002/adma.202211730>.
- [7] M. Kim, J. Chung, T. An, J. Lee, M. Han, S. Lee, W. Choi, J. Kim, S. Han, U. Sim, T. Y. Yu, Paradox of thiourea: a false-positive and promoter for electrochemical nitrogen reduction on nickel sulfide catalysts, *Appl. Catal. B: Environ.* 328 (2023), 122485, <https://doi.org/10.1016/j.apcatb.2023.122485>.
- [8] Y. Kong, Y. Li, X. Sang, B. Yang, Z. Li, S. Zheng, Q. Zhang, S. Yao, X. Yang, L.C. Lei, S. Zhou, G. Wu, Y. Hou, Atomically dispersed Zinc(I) active sites to accelerate nitrogen reduction kinetics for ammonia electrosynthesis, *Adv. Mater.* 34 (2022), 2103548, <https://doi.org/10.1002/adma.202103548>.
- [9] M. Liu, S. Zhang, M. Chen, L. Wu, Boosting electrochemical nitrogen reduction performance through water-in-salt electrolyte, *Appl. Catal. B: Environ.* 319 (2022), <https://doi.org/10.1016/j.apcatb.2022.121925>.
- [10] N. Zhang, G. Zhang, Y. Tian, Y. Guo, K. Chu, Boron phosphide as an efficient metal-free catalyst for nitrate electroreduction to ammonia, *Dalton Trans.* 52 (2023) 4290–4295, <https://doi.org/10.1039/d3dt00551h>.
- [11] X. Shen, S. Liu, X. Xia, M. Wang, H. Ji, Z. Wang, J. Liu, X. Zhang, C. Yan, T. Qian, Interfacial microextraction boosting nitrogen feed for efficient ambient ammonia synthesis in aqueous electrolyte, *Adv. Funct. Mater.* 32 (2022), 2109422, <https://doi.org/10.1002/adfm.202109422>.
- [12] C. Liu, D. Hao, J. Ye, S. Ye, F. Zhou, H. Xie, G. Qin, J. Xu, J. Liu, S. Li, C. Sun, Knowledge-driven design and lab-based evaluation of B-doped TiO₂ photocatalysts for ammonia synthesis, *Adv. Energy Mater.* 13 (2023), 2204126, <https://doi.org/10.1002/aenm.202204126>.
- [13] Y. Liu, L. Wang, L. Chen, H. Wang, A.R. Jadhav, T. Yang, Y. Wang, J. Zhang, A. Kumar, J. Lee, V.Q. Bui, M.G. Kim, H. Lee, Unveiling the protonation kinetics-dependent selectivity in nitrogen electroreduction: achieving 75.05% selectivity, *Angew. Chem. Int. Ed.* 61 (2022), e202209555, <https://doi.org/10.1002/anie.202209555>.
- [14] Z. Wang, J. Liu, X. Wu, N. Nie, D. Zhang, H. Li, H. Zhao, J. Lai, L. Wang, Engineering ordered vacancies and atomic arrangement over the intermetallic PdM/CNT (M = Pb, Sn, In) nanocatalysts for synergistically promoting electrocatalytic N₂ fixation, *Appl. Catal. B: Environ.* 314 (2022), <https://doi.org/10.1016/j.apcatb.2022.121465>.
- [15] M. Wang, S. Liu, H. Ji, J. Liu, C. Yan, T. Qian, Unveiling the essential nature of lewis basicity in thermodynamically and dynamically promoted nitrogen fixation, *Adv. Funct. Mater.* 30 (2020), 2001244, <https://doi.org/10.1002/adfm.202001244>.
- [16] L. Li, W. Yu, W. Gong, H. Wang, C.-L. Chiang, Y. Lin, J. Zhao, L. Zhang, J.-M. Lee, G. Zou, Sulfur-induced electron redistribution of single molybdenum atoms promotes nitrogen electroreduction to ammonia, *Appl. Catal. B: Environ.* 321 (2023), 122038, <https://doi.org/10.1016/j.apcatb.2022.122038>.
- [17] C. Kim, J.Y. Song, C. Choi, J.P. Ha, W. Lee, Y.T. Nam, D.M. Lee, G. Kim, I. Gereige, W.B. Jung, H. Lee, Y. Jung, H. Jeong, H.T. Jung, Atomic-scale homogeneous RuCu alloy nanoparticles for highly efficient electrocatalytic nitrogen reduction, *Adv. Mater.* 34 (2022), e2205270, <https://doi.org/10.1002/adma.202205270>.
- [18] F. Lai, J. Huang, X. Liao, W. Zong, L. Ge, F. Gan, Y. Fang, Y.E. Miao, J. Hofkens, T. Liu, L. Dai, Semicrystalline conjugated polymers with well-defined active sites for nitrogen fixation in a seawater electrolyte, *Adv. Mater.* 34 (2022), e2201853, <https://doi.org/10.1002/adma.202201853>.
- [19] C. Ma, Y. Zhang, S. Yan, B. Liu, Carbon-doped boron nitride nanosheets: a high-efficient electrocatalyst for ambient nitrogen reduction, *Appl. Catal. B: Environ.* 315 (2022), 121574, <https://doi.org/10.1016/j.apcatb.2022.121574>.
- [20] Y. Luo, P. Shen, X. Li, Y. Guo, K. Chu, Sulfur-deficient Bi₂S_{3-x} synergistically coupling Ti₃C₂T_x-MXene for boosting electrocatalytic N₂ reduction, *Nano Res.* 15 (2022) 3991–3999, <https://doi.org/10.1007/s12274-022-4097-9>.
- [21] S. Xu, Y. Ding, J. Du, Y. Zhu, G. Liu, Z. Wen, X. Liu, Y. Shi, H. Gao, L. Sun, F. Li, Immobilization of iron phthalocyanine on pyridine-functionalized carbon nanotubes for efficient nitrogen reduction reaction, *ACS Catal.* 12 (2022) 5502–5509, <https://doi.org/10.1021/acscatal.2c00188>.
- [22] H. Li, M. Xia, B. Chong, H. Xiao, B. Zhang, B. Lin, B. Yang, G. Yang, Boosting photocatalytic nitrogen fixation via constructing low-oxidation-state active sites in the nanoconfined spinel iron cobalt oxide, *ACS Catal.* 12 (2022) 10361–10372, <https://doi.org/10.1021/acscatal.2c02282>.
- [23] M. Liu, Y. Pang, B. Zhang, P. De Luna, O. Voznyy, J. Xu, X. Zheng, C.T. Dinh, F. Fan, C. Cao, F.P. de Arquer, T.S. Safaei, A. Mepham, A. Klinkova, E. Kumacheva, T. Filleter, D. Sinton, S.O. Kelley, E.H. Sargent, Enhanced electrocatalytic CO₂ reduction via field-induced reagent concentration, *Nature* 537 (2016) 382–386, <https://doi.org/10.1038/nature19060>.
- [24] B. Yang, K. Liu, H. Li, C. Liu, J. Fu, H. Li, J.E. Huang, P. Ou, T. Alkayyali, C. Cai, Y. Duan, H. Liu, P. An, N. Zhang, W. Li, X. Qiu, C. Jia, J. Hu, L. Chai, Z. Lin, Y. Gao, M. Miyachi, E. Cortes, S.A. Maier, M. Liu, Accelerating CO₂ electroreduction to multicarbon products via synergistic electric-thermal field on copper nanoneedles, *J. Am. Chem. Soc.* 144 (2022) 3039–3049, <https://doi.org/10.1021/jacs.1c11253>.
- [25] L.D. Chen, M. Urushihara, K. Chan, J.K. Nørskov, Electric field effects in electrochemical CO₂ reduction, *ACS Catal.* 6 (2016) 7133–7139, <https://doi.org/10.1021/acscatal.6b02299>.
- [26] D. Chen, R. Lu, R. Yu, Y. Dai, H. Zhao, D. Wu, P. Wang, J. Zhu, Z. Pu, L. Chen, J. Yu, S. Mu, Work-function-induced interfacial built-in electric fields in Os-OsSe₂ heterostructures for active acidic and alkaline hydrogen evolution, *Angew. Chem. Int. Ed.* 61 (2022), e202208642, <https://doi.org/10.1002/anie.202208642>.
- [27] X.X. Wang, X.Y. Chi, Z.Z. Fu, Y.Y. Xiong, S.Y. Li, Y.B. Yao, K.X. Zhang, Y.J. Li, S. Y. Wang, R. Zhao, Z.Y. Yang, Y.-M. Yan, Interfacial electric field triggered N₂ activation for efficient electrochemical synthesis of ammonia, *Appl. Catal. B: Environ.* 322 (2023), 122130, <https://doi.org/10.1016/j.apcatb.2022.122130>.
- [28] S. Tang, Q. Dang, T. Liu, S. Zhang, Z. Zhou, X. Li, X. Wang, E. Sharman, Y. Luo, J. Jiang, Realizing a not-strong-not-weak polarization electric field in single-atom catalysts sandwiched by boron nitride and graphene sheets for efficient nitrogen fixation, *J. Am. Chem. Soc.* 142 (2020) 19308–19315, <https://doi.org/10.1021/jacs.0c09527>.
- [29] X. Yue, L. Cheng, J. Fan, Q. Xiang, 2D/2D BiVO₄/CsPbBr₃ S-scheme heterojunction for photocatalytic CO₂ reduction: insights into structure regulation and Fermi level modulation, *Appl. Catal. B: Environ.* 304 (2022), 120979, <https://doi.org/10.1016/j.apcatb.2021.120979>.
- [30] J. Zhang, L. Wang, C. Jiang, B. Cheng, T. Chen, J. Yu, CsPbBr₃ nanocrystal induced bilaterial interface modification for efficient planar perovskite solar cells, *Adv. Sci.* 8 (2021), e2102648, <https://doi.org/10.1002/adv.202102648>.
- [31] K. Chu, Y.P. Liu, Y.B. Li, Y.L. Guo, Y. Tian, Two-dimensional (2D)/2D interface engineering of a MoS₂/C₃N₄ heterostructure for promoted electrocatalytic nitrogen fixation, *ACS Appl. Mater. Interfaces* 12 (2020) 7081–7090, <https://doi.org/10.1021/acsm.9b18263>.
- [32] J. Fu, Q. Xu, J. Low, C. Jiang, J. Yu, Ultrathin 2D/2D WO₃/g-C₃N₄ step-scheme H₂-production photocatalyst, *Appl. Catal. B: Environ.* 243 (2019) 556–565, <https://doi.org/10.1016/j.apcatb.2018.11.011>.
- [33] Z.-Y. Liang, J.-X. Wei, X. Wang, Y. Yu, F.-X. Xiao, Elegant Z-scheme-dictated g-C₃N₄ enwrapped WO₃ superstructures: a multifarious platform for versatile photoredox catalysis, *J. Mater. Chem. A* 5 (2017) 15601–15612, <https://doi.org/10.1039/c7ta0433c>.
- [34] Y. Zhang, Z. Gu, J. Bi, Y. Jiao, Molybdenum-iron-cobalt oxyhydroxide with rich oxygen vacancies for the oxygen evolution reaction, *Nanoscale* 14 (2022) 10873–10879, <https://doi.org/10.1039/d2nr02568j>.
- [35] Y. Zheng, T. Zhou, X. Zhao, W.K. Pang, H. Gao, S. Li, Z. Zhou, H. Liu, Z. Guo, Atomic interface engineering and electric-field effect in ultrathin Bi₂MoO₆ nanosheets for superior lithium ion storage, *Adv. Mater.* 29 (2017), 1700396, <https://doi.org/10.1002/adma.201700396>.
- [36] S. Zhao, H.-X. Liu, Y. Qiu, S.-Q. Liu, J.-X. Diao, C.-R. Chang, R. Si, X.-H. Guo, An oxygen vacancy-rich two-dimensional Au/TiO₂ hybrid for synergistically enhanced electrochemical N₂ activation and reduction, *J. Mater. Chem. A* 8 (2020) 6586–6596, <https://doi.org/10.1039/d0ta00658k>.
- [37] Z. Zhu, H. Huang, L. Liu, F. Chen, N. Tian, Y. Zhang, H. Yu, Chemically bonded alpha-Fe₂O₃/Bi₄Mo₃Cl dot-on-plate Z-scheme junction with strong internal electric field for selective photo-oxidation of aromatic alcohols, *Angew. Chem. Int. Ed.* 61 (2022), e202203519, <https://doi.org/10.1002/anie.202203519>.

[38] Y. Lin, C. Yang, S. Wu, X. Li, Y. Chen, W.L. Yang, Construction of built-in electric field within silver phosphate photocatalyst for enhanced removal of recalcitrant organic pollutants, *Adv. Funct. Mater.* 30 (2020), 2002918, <https://doi.org/10.1002/adfm.202002918>.

[39] C. Lv, C. Yan, G. Chen, Y. Ding, J. Sun, Y. Zhou, G. Yu, An amorphous noble-metal-free electrocatalyst that enables nitrogen fixation under ambient conditions, *Angew. Chem. Int. Ed.* 57 (2018) 6073–6076, <https://doi.org/10.1002/anie.201801538>.

[40] Q. Meng, C. Lv, J. Sun, W. Hong, W. Xing, L. Qiang, G. Chen, X. Jin, High-efficiency Fe-mediated Bi_2MoO_6 nitrogen-fixing photocatalyst: reduced surface work function and ameliorated surface reaction, *Appl. Catal. B: Environ.* 256 (2019), 117781, <https://doi.org/10.1016/j.apcatb.2019.117781>.

[41] X. Zhao, X. Li, L. An, L. Zheng, J. Yang, D. Wang, Controlling the valence-electron arrangement of nickel active centers for efficient hydrogen oxidation electrocatalysis, *Angew. Chem. Int. Ed.* 61 (2022), e202206588, <https://doi.org/10.1002/anie.202206588>.

[42] Y. Guo, W. Shi, Y. Zhu, Y. Xu, F. Cui, Enhanced photoactivity and oxidizing ability simultaneously via internal electric field and valence band position by crystal structure of bismuth oxyiodide, *Appl. Catal. B: Environ.* 262 (2020), 118262, <https://doi.org/10.1016/j.apcatb.2019.118262>.

[43] J. Yang, J. Jing, W. Li, Y. Zhu, Electron donor-acceptor interface of TPPS/PDI boosting charge transfer for efficient photocatalytic hydrogen evolution, *Adv. Sci. N.* 9 (2022), 2201134, <https://doi.org/10.1002/adv.202201134>.

[44] Y. Gao, J. Zhu, H. An, P. Yan, B. Huang, R. Chen, F. Fan, C. Li, Directly probing charge separation at interface of TiO_2 phase junction, *J. Phys. Chem. Lett.* 8 (2017) 1419–1423, <https://doi.org/10.1021/acs.jpclett.7b00285>.

[45] Z. Xing, J. Hu, M. Ma, H. Lin, Y. An, Z. Liu, Y. Zhang, J. Li, S. Yang, From one to two: In situ construction of an ultrathin ${}^2\text{D}$ – ${}^2\text{D}$ closely bonded heterojunction from a single-phase monolayer nanosheet, *J. Am. Chem. Soc.* 141 (2019) 19715–19727, <https://doi.org/10.1021/jacs.9b08651>.

[46] J. Zheng, Y. Lyu, M. Qiao, J.P. Veder, R.D. Marco, J. Bradley, R. Wang, Y. Li, A. Huang, S.P. Jiang, S. Wang, Tuning the electron localization of gold enables the control of nitrogen-to-ammonia fixation, *Angew. Chem. Int. Ed.* 58 (2019) 18604–18609, <https://doi.org/10.1002/anie.201909477>.

[47] Y.X. Lin, S.N. Zhang, Z.H. Xue, J.J. Zhang, H. Su, T.J. Zhao, G.Y. Zhai, X.H. Li, M. Antonietti, J.S. Chen, Boosting selective nitrogen reduction to ammonia on electron-deficient copper nanoparticles, *Nat. Commun.* 10 (2019) 4380, <https://doi.org/10.1038/s41467-019-12312-4>.

[48] Y.-C. Hao, Y. Guo, L.-W. Chen, M. Shu, X.-Y. Wang, T.-A. Bu, W.-Y. Gao, N. Zhang, X. Su, X. Feng, J.-W. Zhou, B. Wang, C.-W. Hu, A.-X. Yin, R. Si, Y.-W. Zhang, C.-H. Yan, Promoting nitrogen electroreduction to ammonia with bismuth nanocrystals and potassium cations in water, *Nat. Catal.* 2 (2019) 448–456, <https://doi.org/10.1038/s41929-019-0241-7>.

[49] S. Xue, W. Huang, W. Lin, W. Xing, M. Shen, X. Ye, X. Liang, C. Yang, Y. Hou, Z. Yu, X. Wang, Interfacial engineering of lattice coherency at ZnO - ZnS photocatalytic heterojunctions, *Chem. Catal.* 2 (2022) 125–139, <https://doi.org/10.1016/j.chechat.2021.11.019>.

[50] Y. Liu, Y. Chen, Y. Tian, T. Sakthivel, H. Liu, S. Guo, H. Zeng, Z. Dai, Synergizing hydrogen spillover and deprotonation by the internal polarization field in a MoS_2 / NiPS_3 vertical heterostructure for boosted water electrolysis, *Adv. Mater.* 34 (2022), e2203615, <https://doi.org/10.1002/adma.202203615>.

[51] M. Yuan, J. Chen, Y. Bai, Z. Liu, J. Zhang, T. Zhao, Q. Wang, S. Li, H. He, G. Zhang, Unveiling electrochemical urea synthesis by Co-activation of CO_2 and N_2 with Mott-Schottky heterostructure catalysts, *Angew. Chem. Int. Ed.* 60 (2021) 10910–10918, <https://doi.org/10.1002/anie.202101275>.

[52] Z. Zhu, Q. Lv, Y. Ni, S. Gao, J. Geng, J. Liang, F. Li, Internal electric field and interfacial bonding engineered step-scheme junction for a visible-light-involved lithium-oxygen battery, *Angew. Chem. Int. Ed.* 61 (2022), e202116699, <https://doi.org/10.1002/anie.202116699>.

[53] L. Xu, B. Tian, T. Wang, Y. Yu, Y. Wu, J. Cui, Z. Cao, J. Wu, W. Zhang, Q. Zhang, J. Liu, Z. Li, Y. Tian, Direct Z-scheme polymeric heterojunction boosts photocatalytic hydrogen production via a rebuilt extended π -delocalized network, *Energy Environ. Sci.* 15 (2022) 5059–5068, <https://doi.org/10.1039/d2ee02380f>.

[54] B. Yu, H. Li, J. White, S. Donne, J. Yi, S. Xi, Y. Fu, G. Henkelman, H. Yu, Z. Chen, T. Ma, Tuning the catalytic preference of ruthenium catalysts for nitrogen reduction by atomic dispersion, *Adv. Funct. Mater.* 30 (2019), 1905665, <https://doi.org/10.1002/adfm.201905665>.

[55] N. Zhang, L. Li, J. Wang, Z. Hu, Q. Shao, X. Xiao, X. Huang, Surface-regulated rhodium-antimony nanorods for nitrogen fixation, *Angew. Chem. Int. Ed.* 59 (2020) 8066–8071, <https://doi.org/10.1002/anie.201915747>.

[56] P. Shen, X. Li, Y. Luo, Y. Guo, X. Zhao, K. Chu, High-efficiency N_2 electroreduction enabled by Se-vacancy-rich WSe_{2-x} in water-in-salt electrolytes, *ACS Nano* 16 (2022) 7915–7925, <https://doi.org/10.1021/acsnano.2c00596>.

[57] G. Lin, Q. Ju, X. Guo, W. Zhao, S. Adimi, J. Ye, Q. Bi, J. Wang, M.H. Yang, F. Q. Huang, Intrinsic electron localization of metastable MoS_2 boosts photocatalytic nitrogen reduction to ammonia, *Adv. Mater.* 33 (2021), 2007509, <https://doi.org/10.1002/adma.202007509>.

[58] Q. Dang, S. Tang, T. Liu, X. Li, X. Wang, W. Zhong, Y. Luo, J. Jiang, Regulating electronic spin moments of single-atom catalyst sites via single-atom promoter tuning on S-vacancy MoS_2 for efficient nitrogen fixation, *J. Phys. Chem. Lett.* 12 (2021) 8355–8362, <https://doi.org/10.1021/acs.jpclett.1c02432>.

[59] M. Li, H. Zhu, Q. Yuan, T. Li, M. Wang, P. Zhang, Y. Zhao, D. Qin, W. Guo, B. Liu, X. Yang, Y. Liu, Y. Pan, Proximity electronic effect of Ni/Co diatomic sites for synergistic promotion of electrocatalytic oxygen reduction and hydrogen evolution, *Adv. Funct. Mater.* 33 (2022), 2210867, <https://doi.org/10.1002/adfm.202210867>.

[60] Y. Gu, B. Xi, W. Tian, H. Zhang, Q. Fu, S.L. Xiong, Boosting elective nitrogen reduction via geometric coordination engineering on single-tungsten-atom catalysts, *Adv. Mater.* 33 (2021), 2100429, <https://doi.org/10.1002/adma.202100429>.

[61] X. Yue, L. Cheng, F. Li, J. Fan, Q. Xiang, Highly strained Bi-MOF on bismuth oxyhalide support with tailored intermediate adsorption/desorption capability for robust CO_2 photoreduction, *Angew. Chem. Int. Ed.* 61 (2022), e202208414, <https://doi.org/10.1002/anie.202208414>.